Additive Manufacturing 116 (2026) 105066

Contents lists available at ScienceDirect

Additive Manufacturing

journal homepage: www.elsevier.com/locate/addma

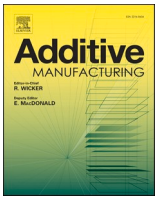

Giant flexoelectricity of additively manufactured polylactic acid☆

Dylan J. Balter [a], Colin McMillen [a], Alec Ewe [b], Jonathan Thomas [b], Samuel Silverman [c], Lalitha Parameswaran [d], Luis Fernando Velásquez-García [e], Emily Whiting [c], Steven Patterson [f], Hilmar Koerner [g], Keith A. Brown [a,b,h,*]

[a] Department of Mechanical Engineering, Boston University, 110 Cummington Mall, Boston, MA 02215, USA
[b] Physics Department, Boston University, 590 Commonwealth Avenue, Boston, MA 02215, USA
[c] Department of Computer Science, Boston University, 665 Commonwealth Avenue, Boston, MA 02215, USA
[d] Lincoln Laboratory, Massachusetts Institute of Technology, 244 Wood Street, Lexington, MA 02421-6426, USA
[e] Microsystems Technology Laboratories, Massachusetts Institute of Technology, 60 Vassar Street, Building 39, Cambridge, MA 02139-4307, USA
[f] Kansas City National Security Campus, 14520 Botts Road, Kansas City, MO 64147, USA
[g] Air Force Research Laboratory, 2941 Hobson Way, Wright-Patterson AFB, OH, USA
[h] Division of Materials Science and Engineering, 15 St Mary's St , Boston, MA 02215, USA

ARTICLE INFO

Keywords:
Additive manufacturing
Flexoelectricity
Microstructure
Strain sensor

ABSTRACT

Flexoelectricity is the electrical response that originates when insulating materials are subjected to a strain gradient. This effect is generally considered to be small but known to depend sensitively on material microstructure. This paper explores the hypothesis that the microstructure produced by additive manufacturing (AM) can strongly influence flexoelectricity. Surprisingly, it is found that minor changes to this microstructure produced using fused filament fabrication, a mainstream approach for additively manufacturing thermoplastics, can lead to enormous changes in the magnitude and polarity of the flexoelectric response of polylactic acid (PLA). To explain these changes, a layer dipole model (LDM) is proposed that connects the in-plane shear in each layer to the electrical polarization that it produces. This model explains three independent mechanisms that were identified and that collectively allow one to drastically increase the flexoelectric effect by 173 fold: (1) choosing printing settings to optimize the geometry of pores between extruded lines, (2) choosing the infill of each layer such that bending-induced strain produces productive in-plane shear stresses, and (3) post-deposition annealing of the printed material to increase its crystallinity. This understanding will enable future sensors in which the structural material is also responsible for electromechanical functionality.

1. Introduction

The conventional wisdom is that when plastics are deformed, they do not generate appreciable electrical potentials. For this reason, sensing deformation of plastics commonly requires the addition of other materials that have distinct sensing functionalities [1–6]. Some polymers do generate potentials through piezoelectricity, but this effect is seldom stronger than their more widely used ceramic cousins [7]. Triboelectric polymer devices leverage charge that can result from relative motion of the materials, though these require interfaces between dissimilar materials [8]. In contrast to these more specialized effects, flexoelectricity is a ubiquitous property of all insulating materials in which strain gradients produce electrical polarization [9–11]. Unfortunately, from a sensing perspective, this effect is extremely weak in polymers. Even the most widely studied material, polyvinylidene fluoride (PVDF), only has a transverse flexoelectric coefficient μ_{12} of 13 nC/m, while the relatively few other flexoelectric studies of polymers, such as with SC-15 epoxy, polyethylene terephthalate, and polyethylene, reveal μ_{12} from 1 to 10 nC/m [12]. Ceramic dielectrics that are more commonly implemented in this field often demonstrate much larger μ_{12}, such as the piezoelectric

☆ This manuscript has been authored by Honeywell Federal Manufacturing & Technologies, LLC under Contract No. DE-NA-0002839 with the U.S. Department of Energy / National Nuclear Security Administration. The United States Government retains and the publisher, by accepting the article for publication, acknowledges that the United States Government retains a nonexclusive, paid-up, irrevocable, world-wide license to publish or reproduce the published form of this manuscript, or allow others to do so, for United States Government purposes.

* Corresponding author at: Department of Mechanical Engineering, Boston University, 110 Cummington Mall, Boston, MA 02215, USA.
E-mail address: brownka@bu.edu (K.A. Brown).

https://doi.org/10.1016/j.addma.2025.105066
Received 29 September 2025; Received in revised form 1 December 2025; Accepted 24 December 2025
Available online 25 December 2025

lead zirconate titanate with a value of 1.4 μC/m [12–14].

Microstructural modifications have been shown to affect the flexoelectric response of a material on a scale comparable to or greater than its intrinsic flexoelectricity. For example, the effective shear flexoelectric coefficient μ_e of lanthanum aluminate crystals increased by 50 % through the introduction of twin boundaries [15]. Furthermore, in experiments with strontium titanate, crystal orientation was discovered to be an important determinant of μ_{12} magnitude and polarity, with values as negative as −5.1 nC/m for one orientation and as positive as 6.1 nC/m for another [16]. Both dislocations and cracks in this strontium titanate crystal structure produced μ_e on the same magnitude, around 3 nC/m, due to large local strains [17,18]. Although flexoelectricity is usually exploited on these smaller scales due to the enhanced strain gradients produced by microstructure, macroscale structural properties can similarly define pronounced flexoelectric responses. For instance, millimeter-size pores in 2-mm thick layers have been observed to enable a flexoelectric signal in polydimethylsiloxane (PDMS) structures under uniform applied strain by creating local strain gradients [19]. To surpass the polarization limit set by bulk properties, fabricating a three-layered, 1.26 mm thick barium strontium titanate device tripled μ_e to 59.5 μC/m, a trend also observed in the porous PDMS sensors when stacking multiple layers [19,20].

While natively controlling such macrostructural designs, additive manufacturing (AM) is also known to strongly influence the microstructure of a material and even provide new degrees of freedom to locally tailor microstructure. For example, it has been widely reported that mechanical properties such as Young's modulus and tensile strength can be modified by manipulating the characteristics of each 3D-printed layer of the structure [21–24]. However, there have been very limited studies focusing on the flexoelectricity of additively manufactured polymers. In one such study, a composite of PVDF with aluminum particles was manufactured using direct ink writing (DIW) to find an increased μ_{12} compared to samples made using casting, although fused filament fabrication (FFF) was not observed to improve flexoelectric properties [13]. A follow-up computational model supported their hypothesis that the increase in voids present in the microstructure of the 3D-printed samples was responsible for the heightened flexoelectricity [25]. However, there is not a consensus on the role of porosity as millimeter-scale pores programmed into FFF-printed design have been reported to have a negligible or negative impact on the μ_{12} of the sample, while micro-scale pores increased μ_e since they do not require as much material to be removed from the structure while still providing amplified strain around the pore [26,27]. Nevertheless, the microstructure control of AM has not yet been found to increase flexoelectricity in a meaningful sense.

Here, we investigate the flexoelectric response of polylactic acid (PLA) coupons through the manipulation of several FFF parameters and find that the AM-induced microstructure plays a major role in determining the flexoelectric response. First, we find that increasing the crystallinity using annealing increases the magnitude of the flexoelectric effect of PLA by a factor of 16. Next, we report the striking observation that the number of printed layers has an enormous impact on the magnitude and sign of the flexoelectric response, with even numbers of layers having a large positive response that grows with layer number while odd numbers of layers have a negative and constant response at μ_{12} = -3.7 ± 2.2 nC/m. To explain these results, we postulate a layer dipole model (LDM) in which the polarization of each layer is determined by the in-plane shear caused by the print direction and the orientation of local voids. This model explains the dependence on layer number, infill direction, and even extrusion multiplier. Finally, we leverage this model to develop coupons in which the flexoelectric effect of each printed layer is aligned and maximized to produce a 173-fold increase in signal over the initially measured samples. Collectively, this work shows how AM-mediated control can dramatically increase the functional properties of common materials and implicates flexoelectricity as a candidate property for advanced sensing applications.

2. Results and discussion

In an initial experiment to test the flexoelectric properties of additively manufactured plastics, rectangular test coupons were 3D printed out of PLA using FFF, affixed with copper tape to form electrodes, and tested using cyclic four-point bending (Fig. 1a-b, further details in methods). In addition to the displacement d recorded by the universal testing machine, the charge Q was recorded using a charge amplifier and then converted to surface charge density σ. This charge amplifier contains a high-pass filter that removes the average charge. Because the sample must be oscillated around a non-zero deformation since we cannot bend the sample upwards, this shifts the zero charge point to the average bending curvature. When tested, a 12-layer PLA sample that had been printed with a cross-hatched linear infill pattern produced a periodic σ that oscillated in phase with d, as expected for a flexoelectric material (Fig. 1c). We computed the bending curvature κ and found a linear relationship between σ and κ with a slope of −3.61 ± 0.78 nC/m (Fig. 1d), which agrees with the theory for a flexoelectric bending test that predicts $\sigma = \kappa\mu_e$ with effective flexoelectric constant μ_e. To verify that this result was not due to triboelectric effects at the interface between the PLA and copper tape, samples with sputtered copper electrodes and copper tape electrodes were compared and found to produce commensurate charge signals (Figure S1).

Having observed a flexoelectric signal in FFF-printed PLA, we sought to study whether post-processing could increase the magnitude of the effect. Specifically, PLA is a semi-crystalline polymer [28–31], and the crystallinity of polymers is known to affect electromechanical properties such as piezoelectricity [32–34]. To test the effect of annealing, identical samples were printed and tested after annealing at varying temperatures for 12 h. Interestingly, μ_e was found to monotonically increase with increasing annealing temperature by as much as a factor of 16 × after annealing at 130 °C to 57 ± 4 nC/m and a factor of 15 × after annealing at 100 °C to 53 ± 16 nC/m (Fig. 1e). This increase in μ_e tracks the increase in crystallinity observed using X-ray diffraction (XRD) (Fig. 1f), which exhibited the peaks expected for crystalline PLA [31]. Interestingly, in addition to increasing in magnitude, μ_e switches signs upon annealing. This shift will be explored in the context of our model of flexoelectricity in additively manufactured PLA (*vide infra*). A p-value of 0.19 was calculated in an unpaired t-test comparing the samples annealed at 100 °C with those annealed at 130 °C, suggesting no statistically significant difference between these data sets. Therefore, the saturation of both crystallinity and μ_e upon annealing at 130 °C suggests that 100 °C is sufficient to maximize the effect of annealing in increasing μ_e. This annealing temperature was thus used for subsequent experiments. To further quantify the crystallinity of the PLA samples, X-ray scattering was performed by the Materials Solutions Network at the Cornell High Energy Synchrotron Source (MSN-C) using microprobe XRD to probe micron-scale heterogeneities introduced by the 3D printing process. The crystallinity maps showed marginal heterogeneities across the layers (Figure S2) and the data revealed an average crystallinity index of 42 % for annealed samples.

After observing that post-processing can drastically increase the flexoelectric signal in FFF-printed polymers, we sought to study whether processing conditions unique to extrusion AM could play a similarly important role. Sample thickness is not expected to play a major role in flexoelectricity for conventionally manufactured materials; however, additive manufacturing introduces additional microstructure due to the layer-by-layer nature of fabrication. To study this, we compared two samples with different numbers of layers n; one with 12 layers and one with 11 layers. Both samples had the same cross-hatched linear infill pattern that began at a 45° angle relative to the long direction of the sample (as shown in Fig. 2a) such that the first 11 layers of both samples were prepared identically, but the 12-layer sample had one additional layer. Strikingly, the maximum σ recorded for the 12-layer sample exceeded 40 nC/m^2 while the maximum σ measured for the 11-layer sample did not exceed 5 nC/m^2 and had the opposite sign (Fig. 2b).

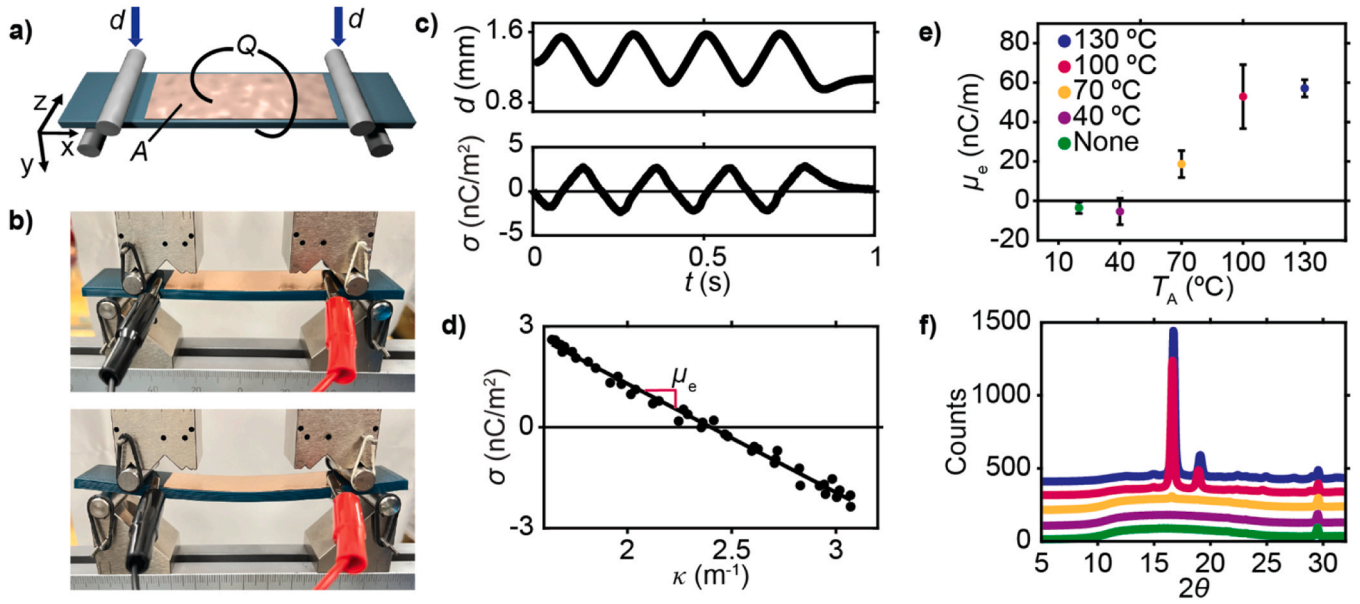

Fig. 1. Experimental apparatus and preliminary flexoelectric characterization of fused-filament-fabrication (FFF)-printed polylactic acid (PLA). a) Diagram of experiment demonstrating 3D-printed PLA samples and copper tape electrodes of area A carrying charge Q where four-point bending rollers apply displacement d. b) Photographs of the experimental setup. c) d and charge density σ vs. time t during one trial. d) σ vs. curvature κ with a linear fit in which the slope is the effective flexoelectric constant μ_e. e) μ_e for different samples annealed at different temperatures T_A. f) X-ray diffraction plots vs scattering angle 2θ for the samples from (e). Each diffraction curve was vertically offset for ease of visualization.

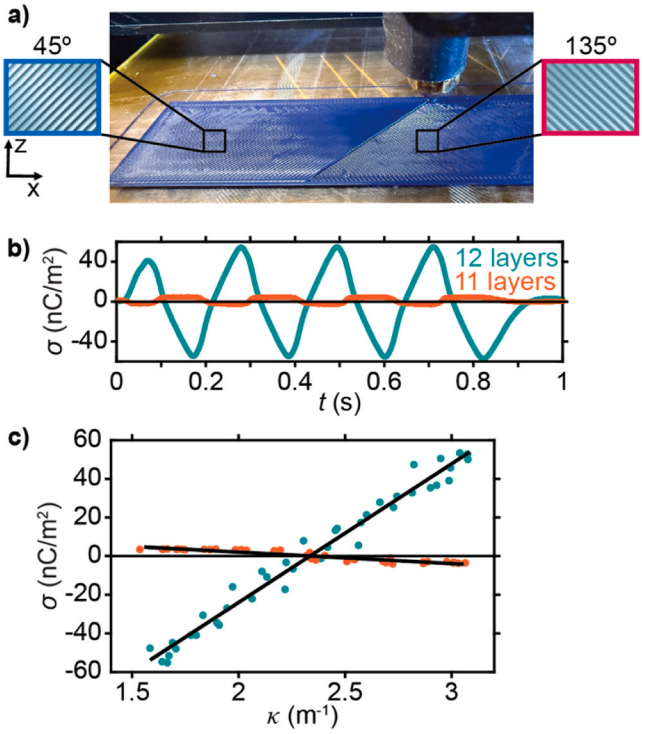

Fig. 2. Dependence of flexoelectricity on number of 3D-printed layers. a) Picture of printing process with infill angles as referenced in the text; a 45° layer is being printed while the underlying 135° layer is partially exposed, illustrating the cross-hatched pattern. b) σ vs. t for an 11- and a 12-layer sample. c) σ vs. κ for an 11- and a 12-layer sample, showing a major difference in both the magnitude and polarity of μ_e.

Despite these surprising results, σ varied linearly with κ for both samples (Fig. 2c). This was a striking result because μ_e is expected to be an intrinsic material property and thus not depend on sample thickness.

In an effort to explain the surprising difference between 12 and 11-layer samples, we construct a model based upon the mechanical anisotropy inherent to FFF-printed samples. Considering a sample being bent by deforming it in the y-axis with the long axis oriented in the x-direction (Fig. 1a), the classic flexoelectric effect is derived from the y-dependence of the x-directed normal strain $\varepsilon_{xx}(y)$. However, it has been widely reported that FFF printing results in mechanical anisotropy with the direction parallel to the tool path being stiffer and stronger [21–24]. We hypothesize that such anisotropy could cause shear or rotation in the xz plane that can vary with y, namely $\varepsilon_{xz}(y)$. Specifically, intuition can be gained by considering a lumped element set of four springs that are fixed at a center point and held at right angles relative to each other (Fig. 3a). Here, the stiffer springs represent the direction along the tool path while the softer springs represent the direction perpendicular to the tool path. When $\phi = 45°$, the system will rotate counterclockwise (CCW) when compressed and clockwise (CW) when pulled in tension. Importantly, the direction of this rotation will reverse for $\phi = 135°$, which is the orientation of the alternating layers of a sample printed with cross-hatched infill.

To further explore this intuition, we use Solidworks to construct a finite element model of a section of one layer (Fig. 3b) and evaluate its behavior when pulled in tension by a unit force distributed across one $y-z$ face of that section. The other $y-z$ face was defined to allow no displacement in the direction of the force and we constrained the center point of that face in all three dimensions. The material is modeled as being a linear elastic isotropic material with an elastic modulus of 2 GPa and a Poisson's ratio of 0.394. Given that Solidworks implements classical strain theory instead of the more comprehensive gradient theory, the distribution of strain in these simulations is examined qualitatively, particularly to consider gradients in strain. In agreement with the simple model, $\varepsilon_{xz} = 0$ if $\phi = 0$, but appreciable ε_{xz} manifests for $\phi = 45°$ that inverts for $\phi = 135°$. In order to understand how these strain fields lead to measurable charge, we consider the flexoelectric constitutive equation that relates the polarization $\vec{P}$ to strain,

$$P_i = \mu_{ijkl}\frac{\partial \varepsilon_{kl}}{\partial x_j}, \tag{1}$$

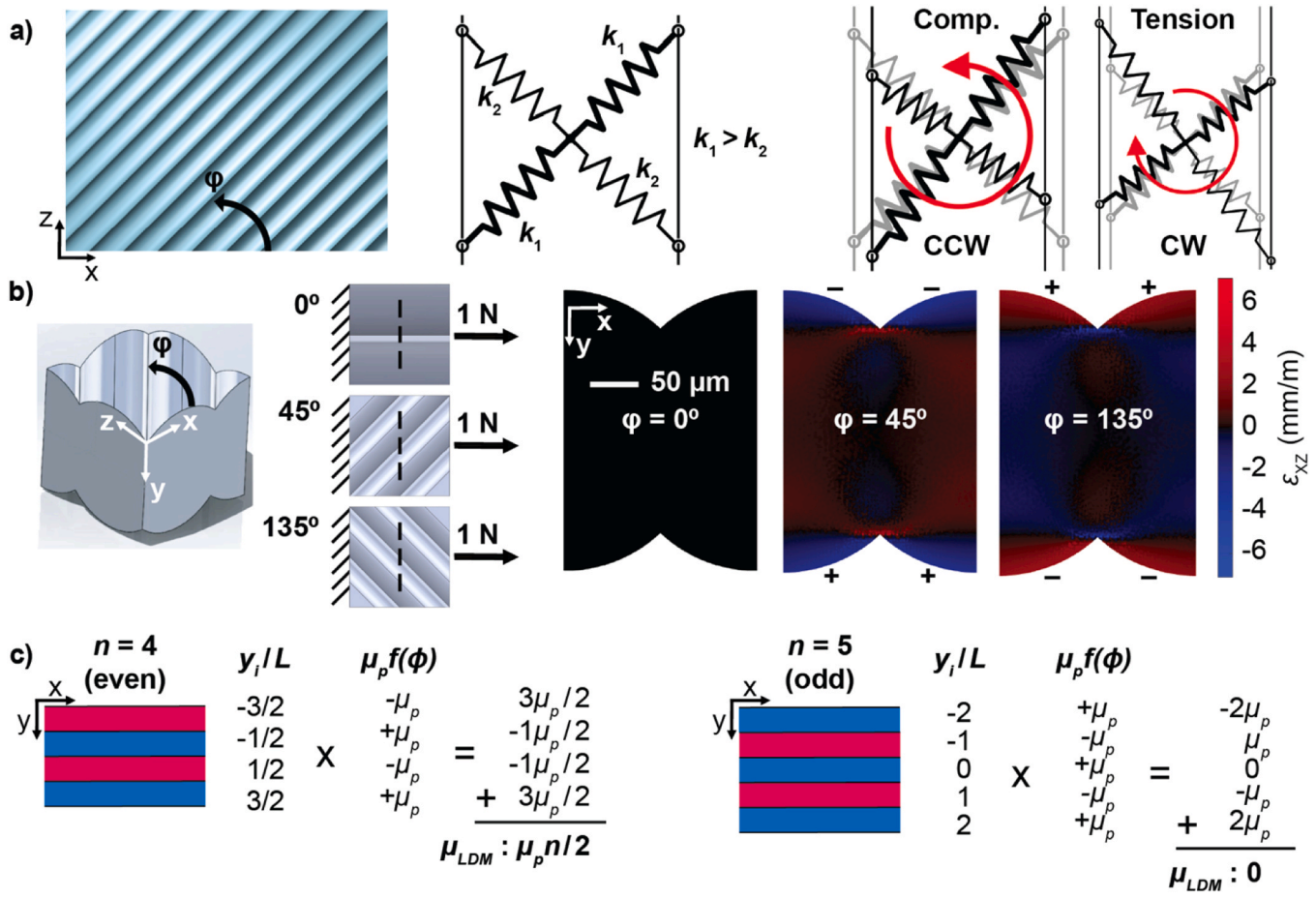

Fig. 3. Depiction of the layer dipole model with its consequences. a) Lumped element model of an individual layer that is stiffer in the tooling direction than perpendicular to it. The tooling path is defined by an infill angle ϕ. This anisotropy leads to rotation whose direction is opposite in compression and tension. b) Finite element analysis of the shear strain ε_{xz} in a section of one layer with a unit force applied on the right side while the left side is held fixed. Images show cross sections for systems with different ϕ. c) Graphical representation of the layer dipole model (LDM) in which the effective shear flexoelectric coefficient of each layer is influenced by the distance to the neutral bending axis, the infill chirality of each layer, and the microstructural impact on ε_{xz}. These dipoles sum to produce the effective shear flexoelectric coefficient μ_{LDM} of the sample.

where we are using the full tensor notation for μ_{ijkl}. For the case where the material is homogenous and isotropic, the charge density σ_y^{hi} measured while bending a sample along the y-axis is,

$$\sigma_y^{hi} = \frac{\mu_{1122}\partial\varepsilon_{xx}}{\partial y} = \mu_{1122}\kappa. \tag{2}$$

We assume that the flexoelectric coefficients are isotropic, therefore the indices defined for μ_{ijkl} are written simply using numbers as indices to reflect the symmetric components of the tensor, following standard convention. Since the bound charge at an air-solid interface is defined by the component of $\vec{P}$ normal to the interface, it is clear that ε_{xz} will play a major role as it changes very dramatically at this interface. Specifically, even in pure tension without the natural strain gradient found in bending, we find that $\partial\varepsilon_{xz}/\partial y$ has large non-zero values at the top and bottom faces of each layer with different signs at the top and the bottom. Further, the sign of the strain gradients switches when ϕ is changed from 45° to 135°. In this way, each layer acts as an electric dipole whose magnitude and sign depend on the layer orientation and the average normal strain in that layer [31]. Since the applied tension in this simulation is arbitrary and not representative of experimental results, we compare these ε_{xz} values to the normal strain ε_{xx} for a $\phi = 0°$ layer (Figure S3), which is constant for all ϕ. The similar magnitudes for both values indicate that ε_{xz} contributes significantly to the total strain profile within a layer for which ϕ is 45° or 135°.

This analysis leads us to postulate a layer dipole model (LDM) of flexoelectricity in FFF-printed plastics in which the total charge is due to the combination of the bulk flexoelectric effect and the contribution from the sheets of dipoles created by each layer. The foundation of the LDM is that the anisotropic voids introduced during printing lead to a mechanical anisotropy that causes appreciable ε_{xz} in each layer and an interface at which charge will accumulate. The dipole sheets cooperatively increase the sample's flexoelectric polarization across each printed layer. We derive an estimate for the charge density σ_y^{LDM} attributed to this mechanical anisotropy that includes the contribution from each of the n layers,

$$\sigma_y^{LDM} = \mu_{1123}\sum_i^n \frac{\int_i \frac{\partial\varepsilon_{xz}}{\partial y} dA}{\int_i dA}. \tag{3}$$

We note that this term depends on the material shear flexoelectric coefficient μ_{1123} and the distribution of ε_{xz}, which is determined by the microstructure of the printed layer. Here, the use of an area average is required to produce the areal charge density. To simplify this equation, we derive an expression for an effective flexoelectric coefficient μ_p from each layer which relies on,

$$f(\phi)\mu_p = \mu_{1123}\ \frac{\int \frac{L}{\langle\varepsilon_{xx}\rangle}\frac{\partial\varepsilon_{xz}}{\partial y} dA}{\int dA}, \tag{4}$$

with

$$f(\phi) = \begin{Bmatrix} 0 & \phi = 0^{\circ} \\ 1 & \phi = 45^{\circ} \\ 0 & \phi = 90^{\circ} \\ -1 & \phi = 135^{\circ} \end{Bmatrix} \quad (5)$$

where L is the height of the printed layer. To produce a simple estimate of this effect, we assume that ε_{xz} in each layer is proportional to the average longitudinal strain, which is $\kappa \cdot y$ from Euler-Bernoulli beam theory assuming $y = 0$ defines the center plane of the beam. Combining this assumption with Eq. (3) and Eq. (4), we find,

$$\sigma_y^{LDM} = \mu_p \kappa \sum_i^n f(\phi) \frac{y_i}{L} \quad = \mu_{LDM} \kappa \quad (6)$$

where y_i is the distance from the neutral strain axis in bending to the center of 3D-printed layer i and μ_{LDM} is the effective shear flexoelectric coefficient of the structure due to both material and microstructural contributions from all 3D-printed layers. This model reveals why samples with even numbers of layers should have a net charge while samples with odd numbers of layers should have no additional charge (Fig. 3c). Interestingly, PLA can also exhibit a shear piezoelectric polarization if it is crystalline with the chains aligned [35,36]. That means that, in addition to the strain gradient which will give rise to a flexoelectric polarization, the presence of shear strains of opposite signs in these layers could mean that potential shear piezoelectricity of crystalline PLA could contribute to the observed polarization. However, X-ray characterization reveals a negligible anisotropy and chain alignment after annealing. Figure S4 shows 2D maps of the order parameter calculated from the anisotropic 2D SAXS pattern using Ruland's method and a map of the angle of crystallite orientation [37]. Based on these results, the order parameter is less than 10 % of a perfectly aligned sample (order parameter of 1) with minor variations across the layers. The angle of orientation changes marginally and tracks the tooling path within the layers. While the X-ray characterization suggests that the PLA lacks the required alignment to exhibit shear piezoelectricity, it is challenging to fully rule this effect out. Thus, future work should include a variety of semicrystalline polymers to understand the interplay between shear piezoelectricity and flexoelectricity. Nevertheless, both potential shear piezoelectricity and the bound charge due to infill-dependent mechanical anisotropy would lead to a polarization that is proportional to the local strain whose sign and magnitude depend on the local microstructure. Using Eq. (2) and Eq. (6), we derive an expression for μ_e as,

$$\mu_e = \mu_{1122} + \mu_p \sum_i^n f(\phi) \frac{y_i}{L}. \quad (7)$$

To explore the ability of the LDM to predict the flexoelectric behavior of FFF-printed PLA, we performed an extensive series of tests varying thickness and infill geometry (Fig. 4a). Initially, we created a series of samples with different thickness with $2 \leq n \leq 13$ in which each of the n layers were 0.292 mm thick (Fig. 4b). In order to obtain results that did not depend on details of the specific roll of filament, we tested three different rolls of filament and printed one sample with each n from each roll, resulting in three samples for each n. This control was meant to mitigate batch-to-batch variation in commercially sourced filament rolls. As predicted by the LDM, all samples with n odd exhibited a negative but constant value of μ_e, which our model predicts should be equal to the effective material property μ_{1122} for annealed PLA which is found to be -3.7 ± 2.2 nC/m by fitting all the data points to Eq. (7). We note that the choice of reporting this as a layer-independent value comes from a test of reduced chi squared that indicated that a more complex model than a constant was overfitting. In contrast with the samples with odd n, the samples with even n exhibited a μ_e that increased linearly with n, which is quantitatively consistent with the LDM that predicts that the flexoelectric magnitude of even-layered cross-hatched samples will grow linearly with n. Thus, these layer-dependent results support the LDM.

Interestingly, the switching of μ_e upon annealing for the 12-layer sample can be explained using the LDM. First, tests of 11-layer cross-hatched samples showed that μ_e became more negative upon annealing. Since the flexoelectricity of these samples are only determined by μ_{1122}, this suggests that annealing does not change the sign of μ_{1122}, but simply increases its magnitude. In contrast, μ_p plays a strong role in the even-layered cross-hatched samples, suggesting that this term is positive and it increases in value upon annealing. Thus, the switching of signs with increasing T_A in Fig. 1e suggests that both flexoelectric terms increase with annealing, but that the influence of μ_p becomes larger than

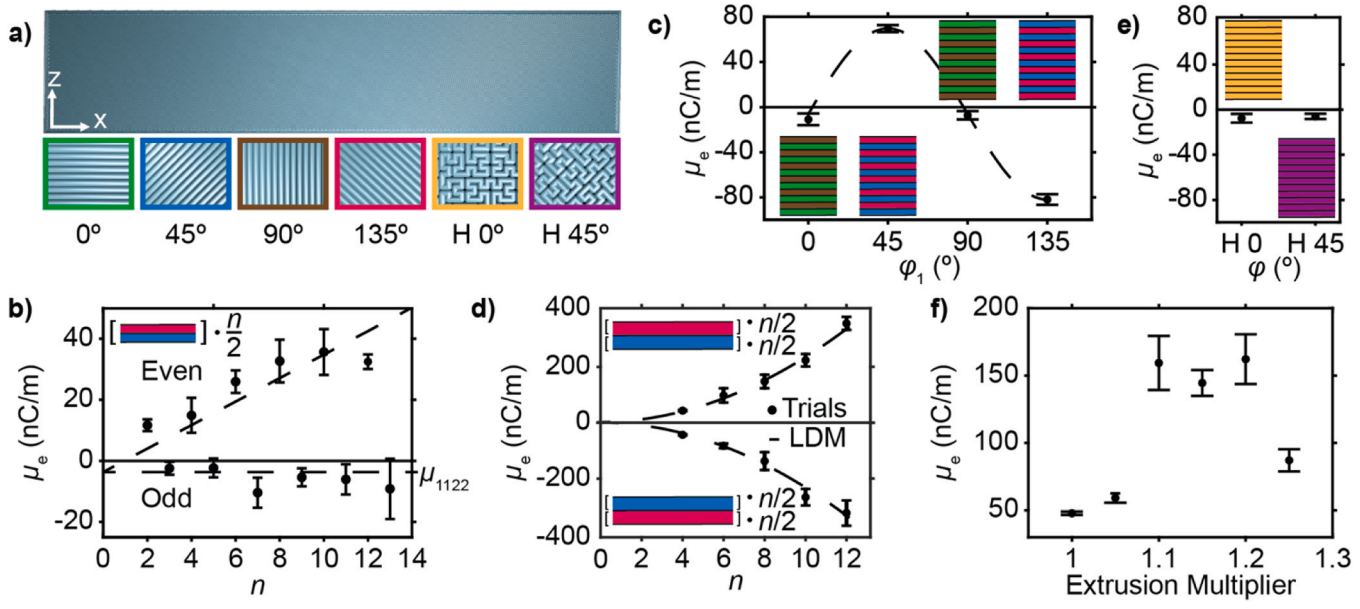

Fig. 4. Experimental validation of the LDM. a) Schematic of a test coupon with insets showing each of the infill types under consideration. b) μ_e vs. number of printed layers n. All data points are fit to Eq. (7), but separate trendlines are shown for even and odd n. c) μ_e vs. first layer infill angle ϕ_1 with sinusoidal fit. d) μ_e vs. n for samples with the first half of their layers all $\phi = 45°$ and the second half all $\phi = 135°$, as well as for this orientation reversed; the plotted fit line is a fit to Eq. (8). e) μ_e vs. ϕ for samples with the Hilbert curve infill pattern. f) μ_e vs. extrusion multiplier for linear cross-hatched samples with n = 12 and $\phi_1 = 45°$.

that of μ_{1122}.

As further verification of the LDM, we created a series of samples with $n = 12$ that varied only in the alignment of the layers. All of these samples featured cross-hatched linear infills but differed in the alignment of the linear paths. Samples that began with $\phi = 0^\circ$ or 90° exhibited very small μ_e, consistent with the PLA material property found in Fig. 4b. Notably, this result shows that pores alone are not enough to enhance flexoelectricity; in-plane rotation is also needed. Further, we compared samples with $n = 12$ that started with $\phi = 45^\circ$ to those that started with $\phi = 135^\circ$ and found that their magnitudes were opposite (Fig. 4c), which agrees with the prediction from the LDM that changing the directions of each layer should change the overall sign of the flexoelectric effect.

Understanding the interaction between strain and chirality led us to study a series of samples that were expected to have notable flexoelectric properties. While adding independent electrodes between each layer would allow the charge to be collected from each layer without any cancellation, the microstructure enabled by additive manufacturing presents other possibilities. In particular, we considered that the symmetry of the longitudinal strain in a bending test means that samples optimized for flexoelectricity should have the same symmetry in their infill orientation. The layers above the neutral plane of the beam should all have the same orientation which should be opposite the orientation of the layers below the neutral plane. This optimized layer sequence would increase flexoelectric polarization while still using just one electrode at the top and one electrode at the bottom of the entire structure. Thus, we designed and tested samples with $n = 12$ in which the first six layers were printed with $\phi = 45^\circ$ and the next six layers were printed with $\phi = 135^\circ$. Indeed, we observed an extremely large μ_e from these optimized samples, with those in which the order of the layers had been swapped exhibiting μ_e with an opposite sign. Specifically, the 45°-first sample exhibited $\mu_e = 450 \pm 18$ nC/m and the 135°-first sample exhibited $\mu_e =$ -520 ± 13 nC/m. As an additional dimension of validation for the LDM, a sequence of trials implementing this optimized infill pattern was performed using even values of n (Fig. 4d). With this optimized layer geometry, Eq. (7) can be used to predict μ_e as,

$$\mu_e = \mu_{1122} + \mu_p\left(\frac{n^2}{4}\right). \tag{8}$$

Eq. (8) fits the experimental results extremely well for both samples in which the first layers were $\phi = 45^\circ$ and samples for which the first layers were $\phi = 135^\circ$. Using this equation as the structure for the fit shown in Fig. 4d, μ_{1122} is calculated as 1.5 ± 5.6 nC/m and μ_p as 9.3 $\pm$ 0.3 nC/m. These numbers are in statistical agreement to analysis of the cross-hatched samples from Fig. 4b using Eq. (7) which revealed that $\mu_{1122} = -3.7 \pm 2.2$ nC/m and $\mu_p = 7.7 \pm 0.8$ nC/m. Contrasting such samples optimized to have large flexoelectricity, we studied samples with space-filling Hilbert geometries oriented either parallel with or at a 45° angle to the edges of the sample. Given that these samples have no net anisotropy in each layer, they would be expected to not exhibit an enhanced flexoelectric signal, as was the case (Fig. 4e). These two samples demonstrated small and negative values of μ_e, namely −7.7 $\pm$ 4.0 nC/m, and -6.0 ± 2.4 nC/m for the 0° Hilbert and 45° Hilbert infills, respectively.

One final consequence of the LDM is that it suggests that the porosity of the printed sample is a key determinant of the measured flexoelectricity. Specifically, because the finite element model is computed using an isotropic material, the only feature that breaks the symmetry is the direction of the pores between FFF-written lines. Experimentally, the pore size can be modified by changing the extrusion multiplier during printing. This property modulates the amount of polymer that is extruded while writing a given line, with higher values being reported to produce smaller pores [38–40]. Interestingly, we found that μ_e increased non-monotonically with extrusion multiplier for samples with $n = 12$ and printed with cross-hatched linear infills starting with $\phi = 45^\circ$. In particular, μ_e dramatically increased to > 150 nC/m and then decreased at extrusion multipliers > 1.2 (Fig. 4f). This suggests that there exists an optimal pore geometry that balances large ε_{xz} (which decreases with increasing extrusion multiplier) with material volume (which increases with increasing extrusion multiplier), though sample printability also becomes a concern at extrusion multipliers > 1.15. Crucially, this result shows that a processing variable unique to additive manufacturing allows μ_e to be increased > 3 fold, showing the power of local microstructure control. Finally, in a complete test of flexoelectric optimization through microstructural manipulation, we annealed samples with $n = 12$ that featured six 45° layers beneath the neutral axis and six 135° layers above and printed with an extrusion multiplier of 1.1. The result was a value of $\mu_e = 625 \pm 102$ nC/m, the largest average μ_e for any test, a 106-fold increase in magnitude from our estimate of the innate μ_{1122} of annealed PLA, and a 173-fold increase from nonannealed $n = 12$ PLA (Figure S5).

3. Conclusion

This work analyzed the complex relationship between microstructure and flexoelectric properties of FFF-printed PLA coupons. We report three distinct ways of increasing the flexoelectric response of FFF-printed PLA that collectively increase the flexoelectric response by as much as 173 fold. Specifically, increasing the crystallinity increased μ_e 15–20 fold, aligning the microstructure further increased μ_e ~8 fold for a 12 layer sample, and modulating the porosity additionally increased μ_e 40 %. We also report the layer dipole model (LDM) that connects this response to the shear in each layer of the printed coupon. Harnessing these three concepts together yielded the largest reported flexoelectric coefficient for an additively manufactured polymer. This study provides a path towards developing strong and flexible mechanical sensors by improving the understanding of the impact that AM parameters have on the flexoelectric properties of polymers. The fact that σ increases as fast as quadratically with the number of layers suggests a direct approach for increasing the charge produced per unit bending for applications such as energy harvesting. If instead, the goal is to optimize the charge produced per unit force, then optimizing the layer thickness, pore geometry, and annealing conditions are crucial. In addition to the fundamental structure-property relationships, this work also highlights the potential for simple and widely available FFF printing to realize high-performance functional materials.

4. Experimental section

4.1. Materials

Samples were printed using dark blue PLA+ filament (eSun) with a 1.75 mm diameter. Copper tape electrodes (Digi-Key) were 25.4 mm in width and cut into 70 mm long strips.

4.2. Sample preparation

A Makergear M2 3D Printer with a nozzle diameter of 0.35 mm was used to print all samples. G-Code for each print was made using Slic3r. The bed temperature was held constant for all prints at 60 °C, while the nozzle temperature was held at 205 °C. The layer height was 0.292 mm, the extrusion multiplier was set to 1 unless otherwise noted, and the nozzle speeds were 60 mm/s for internal perimeters, 30 mm/s for external perimeters, 80 mm/s for the infill, and 80 mm/s for the first layer.

Unless otherwise noted, all samples were placed in an oven after printing and held at 100 °C for 12 h. At the end of the 12-hour annealing cycle, the oven would turn off and cool to room temperature before removing the samples. Samples were tested within 12 h of the annealing cycle. Copper tape electrodes were attached to the top and bottom of the

sample such that they overlapped with a length of 59 mm and width of 25.4 mm.

4.3. Experimental setup

Samples were placed in a four-point bending apparatus connected to a universal testing machine (UTM) (Instron 5965) in which the outer pins were 108 mm apart and the inner pins 86 mm apart. Two alligator clips were attached to the sample such that each only touched one electrode, which was possible because the electrodes were offset instead of being placed directly above one another. The alligator clips were connected to a charge amplifier (VT CAMP-2G05 - Virtins Technology). The four-point bending apparatus was lowered into contact with the sample until the UTM's force measurement increased to 17.5 N to ensure solid contact without slipping during testing. The UTM was programmed to lower by 1.25 mm and wait for several seconds; this step ensured that the charge amplifier reset its measurement to $Q = 0$ C since its built-in high pass filter means that it can only measure changes in charge rather than absolute charge. The UTM was then programmed to oscillate between total displacements of 1.25 and 1.35 mm at a rate of 400 mm/min while the charge amplifier measured Q. The measured displacement d and displacement rate values were measured directly by the UTM. Measurements of Q were all subject to a peak infinite impulse response (IIR) filter to remove common 60 Hz noise, then a low-pass filter at 90 Hz for all other higher frequency noise, such as potential 120 Hz noise from room lights.

4.4. X-ray characterization

The samples were cut into cross sections of thicknesses each measuring 1 mm. The samples were polished using an Allied High Tech Products Inc. MultiPrep System. The wide-angle and small-angle X-ray scattering (WAXS/SAXS) was carried out at the Functional Materials Beamline (FMB) of the Materials Solutions Network at the Cornell High Energy Synchrotron Source (MSN-C) [41]. Measurements were conducted in microprobe mode with an X-ray beam energy of 9.7 keV ($\lambda = 0.128$ nm). The crystallinity index was determined from fits of the WAXS data as described in a previous publication [42]. The order parameter was determined from the anisotropic SAXS patterns using Ruland's method [37].

CRediT authorship contribution statement

Colin McMillen: Writing – review & editing, Investigation. **Dylan J. Balter:** Writing – review & editing, Writing – original draft, Visualization, Validation, Investigation, Formal analysis. **Brown Keith:** Writing – review & editing, Writing – original draft, Visualization, Formal analysis, Conceptualization. **Hilmar Koerner:** Writing – review & editing, Writing – original draft, Investigation. **Steven Patterson:** Writing – review & editing, Funding acquisition, Conceptualization. **Emily Whiting:** Writing – review & editing, Methodology. **Luis Fernando Velásquez-García:** Writing – review & editing, Investigation. **Lalitha Parameswaran:** Writing – review & editing, Investigation. **Samuel Silverman:** Writing – review & editing, Investigation. **Jonathan Thomas:** Writing – review & editing, Investigation. **Alec Ewe:** Writing – review & editing, Investigation.

Declaration of Competing Interest

The authors declare no conflict of interest.

Acknowledgements

KAB, CM, DJB, LP, and LFVG acknowledge support by the Kansas City National Security Campus. This work was partly supported by the National Science Foundation (NSF) under Grant No. REU-2244795. HK would like to thank J Crossno, D Ryan and K Page for collecting data at the Materials Solutions Network at CHESS.

Appendix A. Supporting information

Supplementary data associated with this article can be found in the online version at doi:10.1016/j.addma.2025.105066.

Data availability

The data is present in the manuscript and supporting information.

References

[1] C. Cochrane, M. Lewandowski, V. Koncar, A flexible strain sensor based on a conductive polymer composite for in situ measurement of parachute canopy deformation, Sensors 10 (2010) 8291–8303, https://doi.org/10.3390/s100908291.
[2] M. Amjadi, K.-U. Kyung, I. Park, M. Sitti, Stretchable, skin-mountable, and wearable strain sensors and their potential applications: a review, Adv. Funct. Mater. 26 (2016) 1678–1698, https://doi.org/10.1002/adfm.201504755.
[3] H. Liu, Q. Li, S. Zhang, R. Yin, X. Liu, Y. He, K. Dai, C. Shan, J. Guo, C. Liu, C. Shen, X. Wang, N. Wang, Z. Wang, R. Wei, Z. Guo, Electrically conductive polymer composites for smart flexible strain sensors: a critical review, J. Mater. Chem. C. 6 (2018) 12121–12141, https://doi.org/10.1039/C8TC04079F.
[4] C. Pang, C. Lee, K.-Y. Suh, Recent advances in flexible sensors for wearable and implantable devices, J. Appl. Polym. Sci. 130 (2013) 1429–1441, https://doi.org/10.1002/app.39461.
[5] O. Kanoun, A. Bouhamed, R. Ramalingame, J.R. Bautista-Quijano, D. Rajendran, A. Al-Hamry, Review on conductive polymer/CNTs nanocomposites based flexible and stretchable strain and pressure sensors, Sensors 21 (2021) 341, https://doi.org/10.3390/s21020341.
[6] K.Nath Dhakal, R. Lach, W. Grellmann, B. Krause, J. Pionteck, R. Adhikari, Piezoresistivity and strain-sensing behaviour of poly(butylene adipate- co -terephthalate)/multiwalled carbon nanotube nanocomposites, RSC Adv. 14 (2024) 35715–35726, https://doi.org/10.1039/D4RA04826A.
[7] M. Habib, I. Lantgios, K. Hornbostel, A review of ceramic, polymer and composite piezoelectric materials, J. Phys. Appl. Phys. 55 (2022) 423002, https://doi.org/10.1088/1361-6463/ac8687.
[8] S. Pan, Z. Zhang, Fundamental theories and basic principles of triboelectric effect: a review, Friction 7 (2019) 2–17, https://doi.org/10.1007/s40544-018-0217-7.
[9] L.E. Cross, Flexoelectric effects: charge separation in insulating solids subjected to elastic strain gradients, J. Mater. Sci. 41 (2006) 53–63, https://doi.org/10.1007/s10853-005-5916-6.
[10] L. Shu, R. Liang, Z. Rao, L. Fei, S. Ke, Y. Wang, Flexoelectric materials and their related applications: a focused review, J. Adv. Ceram. 8 (2019) 153–173, https://doi.org/10.1007/s40145-018-0311-3.
[11] S. Baskaran, X. He, Y. Wang, J.Y. Fu, Strain gradient induced electric polarization in alpha-phase polyvinylidene fluoride films under bending conditions, J. Appl. Phys. 111 (2012) 014109, https://doi.org/10.1063/1.3673817.
[12] B. Chu, D.R. Salem, Flexoelectricity in several thermoplastic and thermosetting polymers, Appl. Phys. Lett. 101 (2012) 103905, https://doi.org/10.1063/1.4750064.
[13] M.J. Zaitzeff, L.J. Groven, Flexoelectricity in fluoropolymer/aluminium reactives, Polym. Int. 71 (2022) 829–836, https://doi.org/10.1002/pi.6353.
[14] X. Jiang, W. Huang, S. Zhang, Flexoelectric nano-generator: materials, structures and devices, Nano Energy 2 (2013) 1079–1092, https://doi.org/10.1016/j.nanoen.2013.09.001.
[15] C.A. Mizzi, B. Guo, L.D. Marks, Twin-boundary-mediated flexoelectricity in LaAlO3, Phys. Rev. Mater. 5 (2021) 064406, https://doi.org/10.1103/PhysRevMaterials.5.064406.
[16] P. Zubko, G. Catalan, A. Buckley, P.R.L. Welche, J.F. Scott, Strain-gradient-induced polarization in SrTiO single crystals, Phys. Rev. Lett. 99 (2007) 167601, https://doi.org/10.1103/PhysRevLett.99.167601.
[17] H. Wang, X. Jiang, Y. Wang, R.W. Stark, P.A. van Aken, J. Mannhart, H. Boschker, Direct observation of huge flexoelectric polarization around crack tips, Nano Lett. 20 (2020) 88–94, https://doi.org/10.1021/acs.nanolett.9b03176.
[18] P. Gao, S. Yang, R. Ishikawa, N. Li, B. Feng, A. Kumamoto, N. Shibata, P. Yu, Y. Ikuhara, Atomic-scale measurement of flexoelectric polarization at SrTiO dislocations, Phys. Rev. Lett. 120 (2018) 267601, https://doi.org/10.1103/PhysRevLett.120.267601.
[19] D. Yan, J. Wang, J. Xiang, Y. Xing, L.-H. Shao, A flexoelectricity-enabled ultrahigh piezoelectric effect of a polymeric composite foam as a strain-gradient electric generator, Sci. Adv. 9 (2023) eadc8845, https://doi.org/10.1126/sciadv.adc8845.
[20] S.R. Kwon, W.B. Huang, S.J. Zhang, F.G. Yuan, X.N. Jiang, Flexoelectric sensing using a multilayered barium strontium titanate structure, Smart Mater. Struct. 22 (2013) 115017, https://doi.org/10.1088/0964-1726/22/11/115017.
[21] H. Gonabadi, Y. Chen, A. Yadav, S. Bull, Investigation of the effect of raster angle, build orientation, and infill density on the elastic response of 3D printed parts using finite element microstructural modeling and homogenization techniques, Int. J. Adv. Manuf. Technol. 118 (2022) 1485–1510, https://doi.org/10.1007/s00170-021-07940-4.

[22] S. Ahn, M. Montero, D. Odell, S. Roundy, P.K. Wright, Anisotropic material properties of fused deposition modeling ABS, Rapid Prototyp. J. 8 (2002) 248–257, https://doi.org/10.1108/13552540210441166.
[23] T. Letcher, M. Waytashek, Material Property Testing of 3D-Printed Specimen in PLA on an Entry-Level 3D Printer, in: 2014. https://doi.org/10.1115/IMECE2014-39379.
[24] B. Rankouhi, S. Javadpour, F. Delfanian, T. Letcher, Failure analysis and mechanical characterization of 3D printed ABS with respect to layer thickness and orientation, J. Fail. Anal. Prev. 16 (2016) 467–481, https://doi.org/10.1007/s11668-016-0113-2.
[25] J.H. (Jay) Shin, M.J. Zaitzeff, L.J. Groven, M. Zhou, Microstructure enhancement of macroscopic flexoelectric behavior of THV/Al composites, J. Appl. Phys. 133 (2023) 164101, https://doi.org/10.1063/5.0141173.
[26] M. Zhang, D. Yan, J. Wang, L.-H. Shao, Ultrahigh flexoelectric effect of 3D interconnected porous polymers: modelling and verification, J. Mech. Phys. Solids 151 (2021) 104396, https://doi.org/10.1016/j.jmps.2021.104396.
[27] T.A. Hafner, M. Örnek, D.N. Collard, M.W. Paral, S.F. Son, The effect of porosity on flexoelectricity in 3D printed aluminum/polyvinylidene fluoride composites, J. Appl. Phys. 134 (2023) 194105, https://doi.org/10.1063/5.0173671.
[28] T. Tábi, I.E. Sajó, F. Szabó, A.S. Luyt, Crystalline structure of annealed polylactic acid and its relation to processing, Express Polym. Lett. 4 (2010) 659–668, https://doi.org/10.3144/expresspolymlett.2010.80.
[29] H. Yang, J. Du, Crystallinity, rheology, and mechanical properties of low-/high-molecular-weight PLA blended systems, Molecules 29 (2024) 169, https://doi.org/10.3390/molecules29010169.
[30] T.L. Nguyen, F. Bédoui, P.-E. Mazeran, M. Guigon, Mechanical investigation of confined amorphous phase in semicrystalline polymers: case of PET and PLA, Polym. Eng. Sci. 55 (2015) 397–405, https://doi.org/10.1002/pen.23896.
[31] Y. Srithep, P. Nealey, L.-S. Turng, Effects of annealing time and temperature on the crystallinity and heat resistance behavior of injection-molded poly(lactic acid), Polym. Eng. Sci. 53 (2013) 580–588, https://doi.org/10.1002/pen.23304.
[32] C.S. Lovell, J.M. Fitz-Gerald, C. Park, Decoupling the effects of crystallinity and orientation on the shear piezoelectricity of polylactic acid, J. Polym. Sci. Part B Polym. Phys. 49 (2011) 1555–1562, https://doi.org/10.1002/polb.22345.
[33] B. Mohammadi, A.A. Yousefi, S.M. Bellah, Effect of tensile strain rate and elongation on crystalline structure and piezoelectric properties of PVDF thin films, Polym. Test. 26 (2007) 42–50, https://doi.org/10.1016/j.polymertesting.2006.08.003.
[34] J. Gomes, J. Serrado Nunes, V. Sencadas, S. Lanceros-Mendez, Influence of the β-phase content and degree of crystallinity on the piezo- and ferroelectric properties of poly(vinylidene fluoride), Smart Mater. Struct. 19 (2010) 065010, https://doi.org/10.1088/0964-1726/19/6/065010.
[35] E. Fukada, Bioelectrets and biopiezoelectricity, IEEE Trans. Electr. Insul 27 (1992) 813–819, https://doi.org/10.1109/14.155803.
[36] E. Fukada, New piezoelectric polymers, Jpn. J. Appl. Phys. 37 (1998) 2775, https://doi.org/10.1143/JJAP.37.2775.
[37] W. Ruland, H. Tompa, The effect of preferred orientation on the intensity distribution of (hk) interferences, Acta Crystallogr. Sect. A 24 (1968) 93–99, https://doi.org/10.1107/S0567739468000112.
[38] L. Lendvai, I. Fekete, D. Rigotti, A. Pegoretti, Experimental study on the effect of filament-extrusion rate on the structural, mechanical and thermal properties of material extrusion 3D-printed polylactic acid (PLA) products, Prog. Addit. Manuf. 10 (2025) 619–629, https://doi.org/10.1007/s40964-024-00646-5.
[39] E.G. Gordeev, A.S. Galushko, V.P. Ananikov, Improvement of quality of 3D printed objects by elimination of microscopic structural defects in fused deposition modeling, PLoS One 13 (2018) e0198370, https://doi.org/10.1371/journal.pone.0198370.
[40] M. Sadaf, S. Cano, J. Gonzalez-Gutierrez, M. Bragaglia, S. Schuschnigg, C. Kukla, C. Holzer, L. Vály, M. Kitzmantel, F. Nanni, Influence of binder composition and material extrusion (MEX) parameters on the 3D printing of highly filled copper feedstocks, Polymers 14 (2022) 4962, https://doi.org/10.3390/polym14224962.
[41] L. Smieska, K.A. Page, B. Ree, B. Zheng, H. Koerner, A.R. Woll, The functional materials beamline at CHESS, Synchrotron Radiat. N. 36 (2023) 4–11, https://doi.org/10.1080/08940886.2023.2202578.
[42] B.J. Ree, B. Zheng, A. Abbott, L.M. Smieska, K.A. Page, A.R. Woll, Z. Renwick, H. Koerner, Mapping crystallization kinetics during 3D printing of poly(ether ether ketone), Macromolecules 57 (2024) 2810–2817, https://doi.org/10.1021/acs.macromol.3c02327.